

UC Berkeley

UC Berkeley Previously Published Works

Title

Phase Transformation and Particle-Mediated Growth in the Formation of Hematite from 2-Line Ferrihydrite

Permalink

<https://escholarship.org/uc/item/4z63f2pt>

Journal

Crystal Growth & Design, 16(2)

ISSN

1528-7483

Authors

Soltis, Jennifer A
Feinberg, Joshua M
Gilbert, Benjamin
[et al.](#)

Publication Date

2016-02-03

DOI

10.1021/acs.cgd.5b01471

Peer reviewed

Phase Transformation and Particle-Mediated Growth in the Formation of Hematite from 2-Line Ferrihydrite

Jennifer A. Soltis[†], Joshua M. Feinberg[‡], Benjamin Gilbert[§], and R. Lee Penn[†]

[†]Department of Chemistry and [‡]Institute for Rock Magnetism, Department of Earth Sciences, University of Minnesota, Minneapolis, Minnesota 55455, United States

[§] Earth Sciences Division, Lawrence Berkeley National Laboratory, Berkeley, California 94720, United States

DOI: 10.1021/acs.cgd.5b01471

Publication Date (Web): January 19, 2016

*Address: Department of Chemistry, University of Minnesota, B4, 139 Smith Hall, 207 Pleasant St SE, Minneapolis, MN 55455. E-mail: rleepenn@umn.edu.

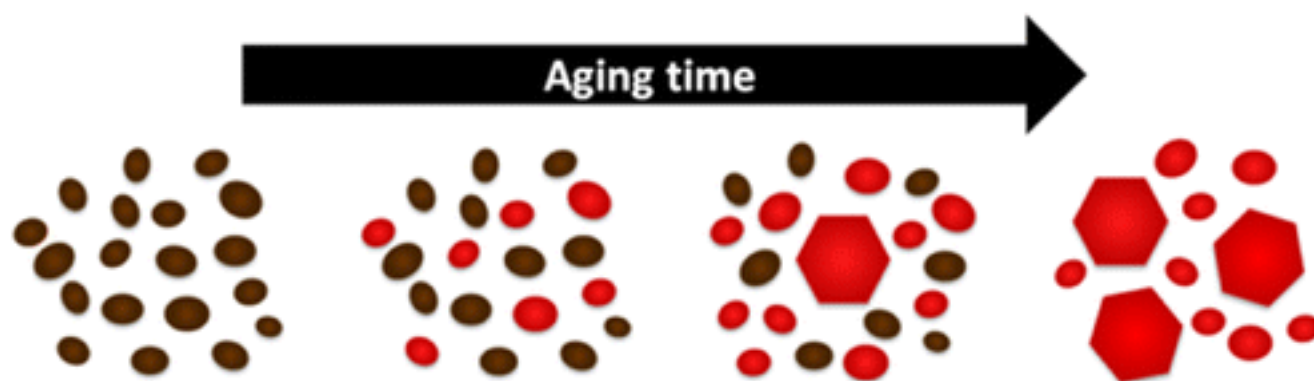
Synopsis

The formation of hematite from 2-line ferrihydrite occurs along several pathways. Material may first phase transform into small hematite particles, followed by particle-mediated growth. 2-line ferrihydrite particles may also aggregate, then form hematite via recrystallization. X-ray diffraction, conventional and cryogenic transmission electron microscopy, preferential dissolution by oxalate buffer, and low temperature SQUID magnetometry were employed to elucidate this process.

Abstract

● 2-line ferrihydrite

● Hematite



Iron oxide nanoparticles are present throughout the Earth and undergo mineral phase transformations that affect their stability and reactivity. The formation of the iron oxide hematite from a 2-line ferrihydrite (2lnFh) precursor requires both phase transformation and growth. Whether phase transformation occurs before or after substantial particle growth, and by which mechanisms particles grow, remain unclear. We conducted time-resolved studies employing X-ray diffraction, room temperature and cryogenic transmission electron microscopy, preferential dissolution by

oxalate buffer, and low temperature SQUID magnetometry to investigate the kinetics and mechanism of hematite formation from 2InFh. A novel form of magnetic measurement was found to be exquisitely sensitive to the presence of hematite, detecting its formation at far lower concentrations than possible with X-ray diffraction. These results indicate that small hematite domains were present even in as-prepared 2InFh suspensions as a side-product of 2InFh synthesis and that the hematite domains increased in size and crystallinity with aging time at elevated temperatures. Second-order kinetics reveals that the hematite growth is consistent with a particle-mediated growth mechanism, possibly oriented attachment.

Introduction

Iron is the most abundant transition metal in the Earth's crust and is required for many life processes. Iron sequestration into, and release from, iron-bearing minerals plays important roles in the movement of iron and energy through the environment. The iron biogeochemical cycle includes a diversity of chemical transformations, from iron precipitation as oxides, sulfides, or other solids to dissolution of iron-bearing solids; transport as dissolved species through soils and groundwater; and abiotic and biotic redox reactions (e.g., biotic reduction by *Geobacter* and *Shewanella*[\(1-3\)](#) and oxidation by *Gallionella* and *Leptothrix*[\(4\)](#) bacteria).

Iron oxide and oxyhydroxide minerals, referred to collectively as the iron oxides, generally have high redox reactivity, high surface activity, and high surface area (frequently $>100 \text{ m}^2/\text{g}$, even for naturally occurring deposits).[\(5\)](#) At all stages of iron oxide growth and phase transformation, these minerals can adsorb and desorb arsenic[\(6\)](#) and heavy metals such as zinc, cadmium, copper, nickel, lead, and manganese,[\(7-10\)](#) facilitate reduction–oxidation reactions at their surfaces,[\(4, 11\)](#) dissolve and reprecipitate,[\(12, 13\)](#) and grow into larger structures.[\(13\)](#) Changes in accessible surface area and surface chemistry due to growth and mineral phase transformations affect the chemical behavior of these minerals in environmental systems. Redox reactivity,[\(14\)](#) solubility,[\(15\)](#) and interactions with heavy metals[\(7, 8, 10\)](#) are just three of many processes that can be affected.

The hydrous ferric oxide ferrihydrite (Fh, $\text{Fe}_5\text{HO}_8 \cdot 4\text{H}_2\text{O}$)[\(5\)](#) is a common early product of both biotic and abiotic precipitation of iron.[\(5, 12\)](#) Fh is a poorly crystalline material that occurs only at the nanoscale and is widely present in the crust, soils, and freshwater and marine systems.[\(12\)](#) Fh is typically classified by the number of peaks observed in its X-ray diffraction patterns, e.g., 2-line or 6-line. It is a precursor to other more crystalline iron oxides, such as hematite (Ht, Fe_2O_3) and goethite

(Gt, α -FeOOH), two of the three most abundant naturally occurring iron oxides, and is metastable with respect to these minerals.[\(5, 12, 16\)](#) Ferrihydrite, goethite, and hematite all share a common framework of hexagonally close-packed oxygen atoms, which supports the idea of pseudomorphic transformations among the three materials.[\(5\)](#) In fact, early work in the crystallography of ferrihydrite hypothesized that it was an extremely defect-laden form of hematite,[\(17\)](#) and there still is no consensus about its exact structure, or how it relates to the structure of hematite.[\(18-27\)](#)

Understanding phase transformations in iron oxides is important for understanding their past and predicting their future interactions with the environment. For example, ferrihydrite is only found in deposits dating from the Pleistocene or younger (<2.6 Mya) because older deposits have already undergone phase transformation into thermodynamically more stable minerals.[\(12\)](#) Two important mechanisms of phase transformation are closely linked to mechanisms of crystal growth. Indeed, phase transformation and crystal growth often occur simultaneously, and it can be difficult to separately characterize each of the contributing mechanisms.[\(28\)](#) Phase transformation by dissolution precipitation (DP) is similar to crystal growth by coarsening, with the mass fraction of the more stable phase increasing at the expense of the dissolving phase. Transformation by interface nucleation (IN) occurs when the new crystal phase nucleates at the interface between two surfaces. The new phase then propagates through the remaining volume of the precursor crystals via solid-state recrystallization.[\(29\)](#) This may be induced by oriented or slightly misoriented alignment of two precursor crystals at a particle–particle interface, similar to the assembly of crystallographically aligned particles in growth by oriented attachment (OA).[\(30\)](#) OA is a nonclassical crystal growth mechanism in which smaller crystals align in a crystallographically ordered manner prior to forming larger crystals[\(31-33\)](#) and has been found to occur in a wide range of mineral systems,[\(31, 34-41\)](#) including the iron oxides.[\(35, 42, 43\)](#) Just as coarsening and OA typically both operate simultaneously but to different extents during crystal growth, so can DP and IN during phase transformation.[\(44-46\)](#)

The transformation from ferrihydrite to both goethite and hematite has been well studied and is dependent on the nature of the Fh (e.g., 2-line vs 6-line), temperature,[\(5, 47-50\)](#) pH,[\(47, 51-53\)](#) and other synthesis conditions.[\(47, 52, 54-57\)](#) For example, at low pH levels, the growth of goethite nanorods from a 6-line Fh (6lnFh) precursor occurs via a multistep mechanism in which primary particles first phase transform and then undergo OA.[\(42, 58\)](#) Though OA is the dominant growth mechanism in the growth of goethite from 6lnFh at low pH, the progressive loss of features like dimples on particle surfaces is evidence for additional growth by coarsening.[\(58\)](#) On the other hand, goethite growth at high pH is dominated by dissolution precipitation.[\(52\)](#)

Phase transformation and growth can also occur when the starting material first assembles into larger structures, then transforms to the new phase, as in the transformation from akaganeite to hematite.⁽⁵⁹⁾ Many iron oxides exhibit size-dependent phase stability, in which changes in particle size and surface area/volume ratio can increase or decrease total free energy.^(16, 60) Phase transformation to hematite is favored when akaganeite particles reach a critical size at which the combined bulk and surface Gibbs free energy of the akaganeite particles is greater than that of hematite particles of similar dimensions.⁽⁵⁹⁾ A complete picture of the factors favoring one growth mechanism over another, or the order of aggregation and phase transformation, remains elusive. Elucidating growth and phase transformation mechanisms for more poorly crystalline 2-line ferrihydrite (2InFh) presents additional challenges due to difficulties associated with imaging poorly crystalline material via transmission electron microscopy (TEM), the ongoing uncertainty over its exact crystal structure,⁽¹⁸⁻²³⁾ and an inability to quantify the material via Rietveld refinement of X-ray diffraction (XRD) patterns.⁽²²⁾ Much past research in phase transformation has drawn heavily upon these techniques (e.g., kinetics of 6-line ferrihydrite to goethite transformation based on TEM,^(54, 61) kinetics and mechanism of phase transformation in titania polymorphs based on XRD data,^(29, 44, 62) and kinetics and mechanism of phase transformation from akaganeite to hematite using data from both XRD and TEM⁽⁵⁹⁾). Because it is difficult or impossible to perform quantitative analysis of 2InFh using TEM or XRD, additional characterization techniques were employed. Low temperature magnetometry is a complementary technique that relies on the use of superconducting quantum interference device (SQUID) sensors to measure induced and/or remanent magnetization of a sample. Low temperature magnetometry has been an important tool in the Earth and materials sciences, but remains underutilized in studies on the fundamentals of nanoparticle growth and phase transformation. Magnetic measurements can provide information about thermally dependent transitions that are diagnostic of mineral identity and can also be used to estimate average particle sizes and the degree of structural order or crystalline defects in a sample.⁽⁶³⁻⁶⁶⁾ SQUID sensors are also exquisitely sensitive to small amounts of magnetic material, particularly for ferromagnetic materials, and can detect mineral concentrations at levels far lower than XRD methods.

In this study, we employ conventional and cryogenic transmission electron microscopy, X-ray diffraction, oxalate dissolution, and low temperature magnetometry to elucidate the mechanism of 2InFh to hematite phase transformation. Magnetic measurements in particular lend critical insight into this system, showing the hematite crystals were present at smaller sizes and lower quantities

than detected previously, and that 2InFh particles possibly undergo phase transformation before assembly into large hematite crystals.

Materials and Methods

Synthesis

All labware was washed in 4 M nitric acid and triple-rinsed with Milli-Q water (Millipore, 18.2 M Ω -cm resistivity) prior to use. Milli-Q was also used for all solutions and dialysis procedures.

Hematite was synthesized following a procedure adapted from Schwertmann and Cornell, Method 6. (67) First, 2-line ferrihydrite (2InFh) was synthesized. While stirring, 300 mL of 0.89 M potassium hydroxide (Mallinckrodt) was added to 500 mL of 0.20 M ferric nitrate (Fisher) in 100 mL aliquots. An additional 200 mL of Milli-Q water was added with sufficient oxalic acid dihydrate (J. T. Baker/Mallinckrodt Baker) to produce a suspension with a total oxalate concentration of 2 mM. The rich brown suspension was stirred for an additional 3 min.

The final suspension was placed into dialysis tubing (Spectra-Por #7 dialysis tubing, MWCO = 2000 g/mol) and dialyzed against Milli-Q water while refrigerated at 10 °C. No more than 250 mL of ferrihydrite was dialyzed per 2 L of Milli-Q water. Water was changed every 1–2 h for four changes and every 4 h for two additional changes. The samples were left in dialysis overnight following the final water change. Dialyzed suspensions were combined and pH adjusted with potassium hydroxide solution such that the final pH was 6.5 when the suspension was mixed with equal volumes of Milli-Q water (pH \approx 5.7).

Samples were aged in a water bath at 90 °C, unless otherwise noted, in a series of 15 mL centrifuge tubes. Each tube was filled with 2.5 mL of Milli-Q water, tightly capped, and placed in the water bath. When the water temperature had reached 90 °C, 2.5 mL of room-temperature 2InFh stock suspension was added to each tube. Tubes were quickly uncapped and recapped during this process to minimize vapor loss. The hot injection step was performed at a rate of three tubes per minute, and the time of 2InFh addition was recorded after every third tube so that the aging time could be adjusted to compensate for the time required perform the hot injection step on each tube. The temperature of the suspensions was monitored by thermometers placed into three additional tubes prepared by the hot injection technique, and these samples reached 90 °C less than 15 min after the injection of 2InFh stock suspension into the hot water. These tubes were equipped with caps that fit closely around the thermometers to prevent changes in temperature due to evaporative cooling.

Three sealed centrifuge tubes were removed from the water bath at each designated sampling time and immediately plunged into an ice bath. Cooling to room temperature or lower took less than 4 min for all samples. Each sample was split into two aliquots: one for analysis via oxalate dissolution and one for drying. The dry samples ranged in color from dark brown (initial) to reddish-orange (final). Two additional samples of 2InFh were prepared with the dialysis step omitted, one with and one without 2 mM oxalate. These samples were freeze-dried by freezing using liquid nitrogen immediately after synthesis and drying under a vacuum in a lyophilizer.

X-ray Diffraction

Dried samples were ground with an agate mortar and pestle and front packed into an aluminum sample holder fitted with a zero-background quartz window. X-ray diffraction (XRD) patterns were collected with a PANalytical X'Pert Pro MPD theta–theta diffractometer with a cobalt K- α source (wavelength 1.79 Å) and an X'Celerator detector over the range of 20–80° 2 θ . The experimental results were compared with the reference powder diffraction file (PDF) for hematite (#33-664). 2InFh does not have a PDF on file with the International Center for Diffraction Data, but it can be identified by the presence of two broad peaks centered at approximately 1.5 and 2.5 Å.[\(18-22, 68, 69\)](#) Line broadening analysis was performed by applying the Scherrer equation[\(70\)](#) to the full width half-maximum measurements of selected peaks obtained from fitting in X'Pert HighScore Plus. Past work using this instrument indicates that a first standard deviation of 10–20% of the calculated particle size is typical when replicate measurements are made of the same sample.[\(62, 71\)](#)

Synchrotron Diffraction

Wide-angle X-ray scattering (WAXS) data were collected at 90 keV (wavelength 0.1080 Å) from powdered samples placed inside hollow Kapton tubes at beamline 11-ID-C of the Advanced Photon Source (APS) at Argonne National Laboratory using a Mar 2D image plate detector. Between 10 and 15 two- or 5 min exposures from an empty tube and each sample were acquired, respectively. The program Fit2D[\(72\)](#) was used to calibrate the detector geometry using data acquired from a Si standard to bin each 2D pattern onto a 1D q axis, where $q = 4\pi \sin \theta/\lambda$, q is the momentum transfer, θ is the scattering angle in degrees, and λ is the wavelength of radiation. The WAXS patterns were scaled prior to subtraction to reveal structural changes with time.

Preferential Dissolution/UV–vis

The method for the preferential dissolution of poorly crystalline iron oxides by ammonium oxalate was adapted from the *Soil Survey Laboratory Methods Manual (SSLMM)*, protocol 4G2a1a2.[\(73\)](#) Aliquots of each suspension were diluted 1:10 with 0.2 M pH 3 ammonium oxalate buffer (oxalic acid (JT Baker) and ammonium oxalate (Sigma-Aldrich)) into microcentrifuge tubes and allowed to sit in

the dark in an ice bath for 3 min. The cold temperature and dark conditions were chosen to prevent dissolution of the more crystalline iron oxides, such as hematite.⁽⁷⁴⁾ The digested samples were then removed from the ice bath and centrifuged for 6 min. The supernatants were collected and analyzed via ultraviolet–visible (UV–vis) spectroscopy. The ammonium oxalate buffer and digested samples were stored in a refrigerator and used or measured within 48 h to minimize growth of microorganisms.⁽⁷³⁾

Supernatants were loaded into 1 cm quartz cuvettes, and the absorbance of 430 nm light was measured using an Agilent 8453 UV–vis spectrometer.⁽⁷³⁾ For solutions too dilute for colorimetric measurements with oxalate, a modified ferrozine assay was performed. The solutions were diluted 1:10 in Milli-Q water, and 100 μL of the diluted solution was added to 900 μL of the ferrozine assay solution, which contained 500 ppm ferrozine (Acros) in 0.2 M ammonium acetate (Fluka) and 5 mM ascorbic acid (Acros). Each sample was prepared in triplicate, and absorbance was measured at 562 nm. The addition of ascorbic acid results in the reduction of dissolved Fe(III) to Fe(II), which makes the assay sensitive to total iron, rather than selective to Fe(II).⁽⁷⁵⁾ The dissolved iron in these solutions is expected to be entirely Fe(III).

In both cases, calibration curves were constructed from absorbance measurements of ferric nitrate standard solutions in oxalate buffer or the ferrozine assay solution.

Transmission Electron Microscopy

Transmission electron microscopy (TEM) images were collected using an FEI Tecnai T12 microscope operating at 120 kV or an FEI Tecnai G² F30 microscope operating at 300 kV. Both microscopes are equipped with Gatan charge-coupled device (CCD) cameras and use Gatan Digital Micrograph v3 to process images. Further image analysis was performed using ImageJ (v1.43m and later), a public domain NIH image processing and analysis program written by Rasband.

⁽⁷⁶⁾ Specimens were prepared by diluting 20 μL of sample into 3 mL of Milli-Q water, sonicating for 30 s, and placing a single drop of diluted suspension onto the carbon-coated side of a 200 mesh Cu holey carbon grid (Structure Probe, Inc.). Grids were allowed to dry under ambient temperature and humidity.

Cryogenic (cryo) TEM specimens were prepared using a Vitrobot (FEI Mark IV) under 100% relative humidity. A 2InFh suspension aged at 90 °C for 6 h was previously quenched in an ice bath and taken directly to the microscopy preparation lab. One specimen was vitrified without further treatment. The second was treated via the oxalate dissolution process as described above and vitrified 7 min after mixing with oxalate buffer (samples prepared for Fe(III) analysis had a total exposure time to oxalate buffer of 9–10 min).

Three microliters of suspension were placed onto a 200 mesh Cu lacy carbon grid (Structure Probe, Inc.), blotted with filter paper for 2 s, and plunged into liquid ethane ($-183\text{ }^{\circ}\text{C}$) to vitrify the water and form a relatively electron-transparent solid. The grid was then transferred to a storage box held under liquid nitrogen ($-178\text{ }^{\circ}\text{C}$). All subsequent handling of the prepared grids occurred under liquid nitrogen to maintain cryogenic conditions. Samples were imaged using an FEI Tecnai G² F30 TEM fitted with a cryogenic sample stage and operated at 300 kV. Images were collected with a Gatan charge-coupled device (CCD) camera using Gatan Digital Micrograph.

Preparation of Samples for Magnetic Measurements

The dried, ground samples were prepared for magnetic measurements after XRD patterns had been collected. At least 100 mg of each sample was tightly packed into a gelatin or cellulose capsule. Powdered sugar was used as a filler material to prevent unwanted vibration in samples with low sample volume. The sample capsules were tared before loading and massed before the addition of powdered sugar to obtain accurate iron oxide mass measurements.

Magnetic Measurements

All magnetic measurements were performed at the Institute for Rock Magnetism, University of Minnesota, using a Quantum Designs Magnetic Properties Measurement System instrument (MPMS-5S). Samples were first imparted with a 2.5 T room temperature saturation remanent magnetization. The 2.5 T field was then turned off, and the intensity of the remanent magnetization was measured during cooling from room temperature to 20 K and then back to room temperature in the presence of either a $\pm 5\text{ mT}$ DC field. While it is possible to collect measurements in the MPMS using a “zero-field” environment, in reality there are often small, temporally variable residual fields that can create unwanted induced magnetizations in magnetic samples. It is possible to minimize these residual fields to a value $<0.5\text{ mT}$ prior to the beginning of an experiment; however, this calibration process is time-consuming and is often rendered inaccurate after a 2.5 T field is produced. The 5 mT DC fields used in this study allow us to create a controlled, repeatable magnetic environment in which to measure the samples. An example of raw data as collected from the SQUID magnetometer is shown in [Figure 1A](#).

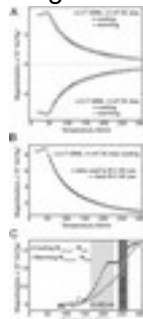


Figure 1. An explanatory figure to demonstrate how magnetic data is processed. (A) The raw data as it is collected from the SQuID magnetometer. The 2.5 T room temperature saturation magnetization is measured during thermal cycling from 300 to 20 to 300 K in the presence of a positive or negative 5 mT DC bias field. (B) An example of fitting a Curie–Weiss relationship to a subset of the data that is detected almost entirely by the superparamagnetic ferrihydrite in the sample. (C) The residual magnetization in the sample (+5 mT DC bias) after the contribution to magnetization from ferrihydrite has been removed. The dark gray box shows the 240–265 K range of observed Morin transitions for grains ≥ 100 nm.[\(65\)](#) The light gray box shows the 165–230 K range of observed Morin transitions for grains ≤ 90 nm.[\(65\)](#)

Magnetic data collected during thermal cycling were then fitted with a Curie–Weiss Law relationship. There are several formulations of the Curie–Weiss relationship, and here we used the following, which is optimized for data collected right up to a material’s blocking temperature, $M = a/(T - b)^c$ where the specimen’s magnetization, M , is defined as the inverse relationship with temperature, T . The coefficients a , b , and c are parameters that are fit to the data. Earlier studies on the magnetic properties of similar superparamagnetic ferrihydrite calculated blocking temperatures of ~ 35 K.[\(77, 78\)](#) A Curie–Weiss relationship was fitted to data collected between 55 and 130 K, which corresponds to the interval that showed the most pronounced effects of ferrihydrite’s magnetic blocking. It also avoided any data contamination from hematite, which is thought to only have a minor defect moment at temperature below the Morin transition.

If the ferrihydrite samples in this study were simply collections of superparamagnetic ferrihydrite, then the Curie–Weiss relationships would fit the data above 130 K very well. However, as can be seen in [Figure 1B](#), the Curie–Weiss relationship does not fit all of the data at temperatures above 130 K. The difference between this theoretical magnetic behavior and the data is primarily the effect of trace quantities of hematite in the sample. [Figure 1C](#) shows an example of the how the magnetic data were processed and how a nonspecialist in magnetic methods should interpret the results. Changes in slope between the cooling and heating curves observed in the 240–265 K range indicate Morin transitions associated with hematite grains ≥ 100 nm, while those in the 165–230 K range indicate the Morin transitions for grains ≤ 90 nm.[\(79\)](#)

Results and Discussion

Major Phase Composition

XRD results ([Figure 2](#)) demonstrate that the amount of hematite increased and ferrihydrite decreased with time at 90 °C, until the sample consisted of pure hematite. In the unaged (0 h) sample, only 2lnFh peaks are visible.

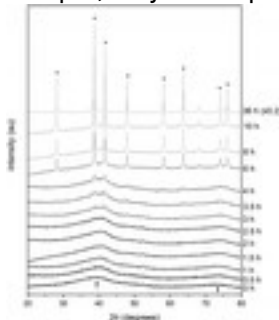


Figure 2. X-ray diffraction patterns of samples collected after aging a suspension of 2-line ferrihydrite at pH 6.5 and 90 °C for 0–10 h. Co K- α radiation was used to collect the patterns. Diffraction peaks for 2-line ferrihydrite are indicated with arrows (no PDF). Peaks for hematite are indicated with * (PDF #33-664). Peaks at 53° 2 θ are background peaks from the Al sample holder. Patterns are vertically offset for clarity.

Low-intensity peaks for hematite are first visible after 2.5 h of aging, and only hematite peaks are present after 10 h. Some, but not all, samples had detectable hematite after 2 h of aging. The color of the nanoparticle suspensions changed from dark brown to red orange as hematite content increased.

XRD patterns further demonstrate that the hematite crystal size increases with aging time. The size of the crystals along several crystal directions, quantified by XRD line broadening analysis using the Scherrer equation,⁽⁷⁰⁾ are shown as a function of aging time in [Figure 3](#). Measurements from experiments performed using two batches of 2lnFh show an increase in crystal size along the Ht (012), (104), and (110) planes and are in good agreement.

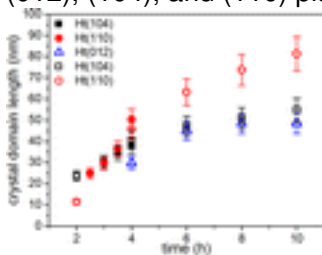


Figure 3. Hematite crystal domain lengths along (012), (104), and (110) as a function of aging time, with two different batches of ferrihydrite (open and closed symbols) used as the starting material. Error bars represent 10% of the calculated domain length and approximate the first standard deviation.^(62, 71)

Synchrotron X-ray diffraction measurements are also consistent with increasing hematite content ([Figure 4](#)). Difference patterns were obtained by subtracting the synchrotron diffraction pattern of an

unheated 2lnFh sample from the patterns for aged samples (0.5–4.0 h). The small shoulder at ca. 2.4 \AA^{-1} after 2.5 h of aging is the first indication of hematite in the sample, and this shoulder coincides with the most intense of the peaks (at 2.3 \AA^{-1}) in the synchrotron diffraction pattern of pure hematite, which is shown at the bottom of [Figure 4](#). The hematite peaks beginning to emerge in the difference patterns can be compared to the diffraction pattern for pure Ht aged for 36 h (not a difference pattern) at the bottom of the figure.

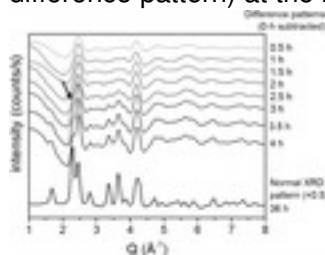


Figure 4. Synchrotron X-ray diffraction patterns of 2-line ferrihydrite aged at pH 6.5 and $90 \text{ }^\circ\text{C}$. The pattern for pure hematite (aged for 36 h) is shown at the bottom. Difference XRD patterns for samples aged 0.5–4 h are shown above and were calculated by subtracting the 0-h pattern from the measured pattern for each aged sample. The first visible shoulder, indicating the presence of a small amount of hematite, is marked with an arrow in the 2.5-h sample.

X-ray diffraction methods typically have detection limits of ca. parts per thousand, at best. Thus, magnetic measurements, which can have substantially lower detection limits, were employed to quantify hematite in samples collected at earlier times. Hematite can most clearly be observed in low temperature magnetometry by its Morin transition (T_M), which is observed as a sudden decrease in magnetization during cooling as magnetic moments change from oriented within the mineral's basal plane at temperatures $> T_M$ to oriented normal to the basal plane at temperatures $< T_M$. There is a grain-size dependence to the Morin transition, with grains $\geq 100 \text{ nm}$ displaying magnetization loss between 240 and 265 K, while grains $\leq 90 \text{ nm}$ yield T_M between 165 and 230 K.[\(65\)](#) In general, T_M also shifts to lower temperatures when particles have high internal strain, high surface to volume ratios, are doped with non-Fe cations, or have high levels of defects.[\(64\)](#) Finally, hematite grains that are exceedingly small or defect-rich can exhibit significant thermal hysteresis in T_M between heating and cooling.[\(65\)](#)

As with the XRD results, magnetic measurements show the mass fraction of hematite increased with aging time. Magnetization curves for 2lnFh synthesized and aged under different conditions are displayed in [Figure 5](#). Magnetic measurements demonstrate that suspensions of ferrihydrite prepared with 2 mM oxalate, air-dried, and aged at $90 \text{ }^\circ\text{C}$ for 0–3 h show that hematite content, particle size, and crystallinity increase with time ([Figure 5C–F](#)). Each of the aged samples displays

Morin transitions that are consistent with hematite grain size distributions include both larger grains (≥ 100 nm) that would produce standard T_M as well as smaller grains (≤ 90 nm) that would produce depressed T_M values. The magnetic contributions from small grains are more significant in samples aged for shorter times. It is also notable that the difference between the cooling and heating cycles becomes negligible as aging times increase, suggesting that the extent of crystalline defects decreases in samples that have been aged for longer periods. In similar syntheses, the earliest formation of hematite detectable via XRD did not occur until the suspension had been aged for 2.5 h.

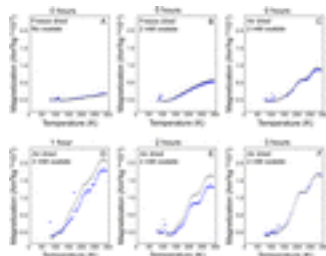


Figure 5. Temperature vs residual magnetization upon cooling (gray dots) and heating (blue dots) for differently aged 2-line ferrihydrite. Top row: Samples prepared without any aging at elevated temperature. Left: 2InFh prepared without oxalate and freeze-dried immediately after synthesis. Middle: 2InFh prepared in the presence of 2 mM oxalate and freeze-dried immediately after synthesis. Right: 2InFh prepared in the presence of 2 mM oxalate, dialyzed at 10 °C for 24 h, and air-dried at room temperature. Bottom row: 2InFh prepared in the presence of 2 mM oxalate, dialyzed at 10 °C for 24 h, aged for 1–3 h at 90 °C, and air-dried at room temperature.

Both air-drying and the use of oxalate during synthesis were found to increase the amount and crystallinity of hematite formed. A T_M , albeit with very low magnetization, is identifiable even in the oxalate-free, freeze-dried 2InFh sample (Figure 5A), showing that a trace amount of small, defect-rich hematite nanoparticles is present in the as-synthesized Fh. This demonstrates that hematite is nucleating during the synthesis of the 2InFh precursor at levels that were undetectable by either X-ray diffraction technique.

Oxalate is commonly used in hematite syntheses and may promote hematite formation.^(57, 67, 80) The addition of 2 mM oxalate to a 2InFh synthesis that was subsequently freeze-dried increased the amount of hematite formed and decreased its level of crystal defects (Figure 5B), and air-drying a similar suspension further increased the amount and crystallinity of the hematite produced (Figure 5C). This can be seen by an increase in residual magnetization and the amount of hysteresis between cooling and heating. We conclude that some phase transformation occurred during the days-long air-drying process.

Increased magnetization at ca. 120 K, which was observed in several of the samples, corresponds with the Verwey transition diagnostic of magnetite (Fe_3O_4).⁽⁶³⁾ Because of magnetite's strong ferrimagnetic character, signals of this amplitude may be due to the presence of only a single grain of magnetite. There was no source of Fe(II) in the 2InFh synthesis and very low quantities of compounds with any reducing capacity (2 mM oxalate). Additionally, all syntheses and reactions were performed in air, making the formation of magnetite during synthesis unlikely. Therefore, the magnetite signal is attributed to very low levels of contamination (e.g., one to several nanoparticles).

Particle Shape and Aggregation State

TEM images (Figure 6) of samples aged for 0–6 h also show that hematite content increases with aging time. Initially, little diffraction contrast is observed in the large aggregates of primary particles, and diffraction contrast of the primary particles increases with aging time. The unaged and 2-h sample are very similar in appearance, even though magnetic results indicate that small hematite particles are present in greater amounts after aging. After 3 h, hematite particles were visually identifiable in the images. Lattice fringes visible in the high-resolution image (Figure 6, middle right) have spacing consistent with hematite (012) planes. Though the hematite particles appear to have a wide range of morphologies, they are actually relatively monodisperse; a tilt series of TEM images showed that a single particle could appear rhombahedral, hexagonal, or irregularly shaped depending on its orientation relative to the electron beam (Figure S1).

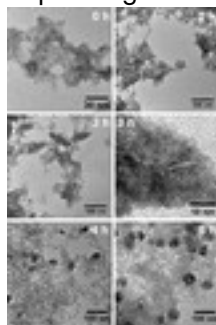


Figure 6. Time-resolved TEM images from the synthesis of hematite from an aqueous suspension of 2-line ferrihydrite aged at 90 °C. At 0 and 2 h, only primary particles are visible. After 3, 4, and 6 h, a mixture primary particles and large hematite crystals can be seen. Three hour sample, right image: The earliest sample in which hematite could be identified, based on lattice fringe spacing, was 3 h. The white line parallels the hematite (012) lattice fringes.

Aggregation of nanoparticles is a common drying artifact of conventional TEM specimen preparation, so an in situ technique, such as cryo-TEM, is needed to gain insight into the actual aggregation state of the particles in suspension. Figure 7 shows a cryo-TEM image of a specimen vitrified after 6 h of aging. The primary particles were highly aggregated, and large hematite crystals were always seen

in proximity to these fractal-like structures. The small particles have a wide range of contrast, which is most likely the consequence of diffraction contrast. Thus, we conclude that there is a range of crystallinity in the small particles. The hematite crystals in the higher-magnification inset appear to be made up of many small subunits, consistent in size with the primary particles, and are relatively uniform in contrast, which would be expected if the particles were crystallographically aligned (perhaps through OA). A small amount of nanorods was also seen, consistent in shape with goethite,[\(5, 42\)](#) but goethite was not detected by any of the other characterization techniques.

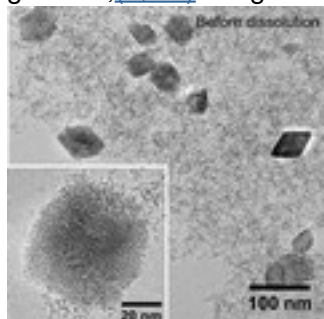


Figure 7. Cryo-TEM images of 2InFh aged for 6 h at 90 °C prior to vitrification. Primary particles—likely a mix of 2InFh and hematite—and high-contrast, 30–80 nm hematite particles are both visible in the sample vitrified after 6 h of aging. Inset: higher magnification image showing texture of a large hematite particle.

Kinetics

The consumption of primary particles—2InFh and similarly sized hematite—in the formation of large hematite crystals was measured using preferential dissolution by an oxalate buffer. Preferential dissolution by oxalate is commonly used in soil science to determine the content of poorly crystalline iron in a soil sample by exploiting the difference in dissolution rates between poorly crystalline and well-crystalline iron-containing minerals (e.g., $k_{2\text{InFh}} \gg k_{\text{hematite}}$).[\(15, 73\)](#) Small hematite particles also dissolve more rapidly than larger ones, presumably due to their higher surface area and an increase in surface structural disorder ([Figure S2](#)). The amount of dissolved Fe(III) is proportional to the amount of iron contained in primary particles and can be used to determine the rate at which primary particles are consumed to form large hematite particles.

Linear trends in a plot of inverse $\text{Fe(III)}_{\text{aq}}$ concentration vs time ([Figure 8A](#)) indicate that the consumption of primary particles follows a second-order rate law. This is consistent with a particle-mediated crystal growth mechanism, such as OA. Consumption of primary particles was also found to be more rapid when 2InFh suspensions were aged at 90 °C, rather than 77 °C, showing that the rate of this reaction is temperature-dependent. Though the mineral phase cannot be determined from oxalate dissolution alone, a pellet consistent in color with the final hematite suspensions was visible to the eye after centrifuging a sample that had been aged for 0.5 h at 90 °C and treated with

the preferential dissolution process. This shows that preferential dissolution via oxalate can be used to detect non-ferrihydrate phases at concentrations detectable only by SQUID magnetometry and undetectable by the X-ray diffraction techniques.

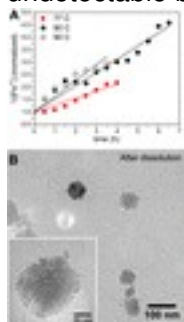


Figure 8. (A) Inverse concentration of Fe(III) (aq) after preferential dissolution by oxalate as a function of aging time for samples aged at 77 (solid squares) and 90 (solid and open diamonds) °C. [Fe(III)] is directly proportional to the concentration of primary particles remaining at each sampling time. (B) Cryo-TEM image of a sample treated with the preferential dissolution process for 7 min prior to vitrification. Many large hematite particles remain, but few primary particles are visible.

Cryo-TEM images of a suspension aged for 6 h at 90 °C and treated with the preferential dissolution procedure before vitrification ([Figure 8B](#)) show hematite crystals consistent in shape and size with the predissolution sample ([Figure 7](#)) and the conventional TEM images. Very few small particles can be seen, leading us to the conclusion that preferential dissolution by oxalate buffer was effective at dissolving primary particles.

Implications for Phase Transformation and Growth

The formation of small hematite particles could occur along many possible pathways. Small hematite domains were observed in the as-synthesized 2InFh, which could provide nucleation sites for the propagation of hematite throughout an aggregate in a solid-state phase transformation. This is similar to the final steps of the proposed model of akaganeite to hematite transformation presented by Frandsen and Legg et al., in which additional akaganeite particles aggregate onto large hematite particles and then phase transform.⁽⁵⁹⁾ On the other hand, ferrihydrate could transform into small hematite particles, which then assemble via OA, as broadly proposed by Lin et al. (2013). In this case, transformation could be induced via interface nucleation (IN) if two particles made transient contact and formed an interface at which the new phase could nucleate, but did not form particle–particle bonds before disaggregating. Hematite growth could also occur by the dissolution of ferrihydrate and precipitation of the dissolved species onto pre-existing hematite nuclei. Finally, the formation of hematite from the aggregation of ferrihydrate particles followed by solid-state phase

transformation cannot be ruled out as an additional pathway concurrent with one or more of the others proposed.

Our data support several of these possible pathways. The texture of the hematite particles observed in TEM images supports a particle-mediated growth mechanism ([Figures 6, 7, and S2](#)) and only rules out DP as the dominant route of hematite formation. Peak broadening analysis ([Figure 3](#)) indicates that >20 nm hematite particles are present as early as 2 h of aging. The XRD data could indicate that ferrihydrite aggregated into large structures prior to transformation or that small hematite particles had already assembled into a larger structure via a process such as OA. The observed diffraction contrast in TEM images ([Figures 6 and 7](#)) suggests that small crystalline particles formed prior to aggregation into larger structures. The hematite structural intermediates seen in [Figures 7 and 8b](#) (insets) are reminiscent of the structural intermediates interpreted as evidence for OA in goethite crystal growth in which phase transformation precedes aggregation. ([42, 81](#)) Magnetometry results also support the hypothesis that small hematite particles form first, followed by aggregation.

With the exception of DP, all of the proposed mechanisms are types of particle-mediated growth and would be consistent with a second order rate law, ([31](#)) as observed via preferential dissolution ([Figure 8a](#)). Particles may assemble before or after phase transformation. DP and coarsening may also play a role, e.g., by filling in the dimpled surfaces of the large hematite nanoparticles, such as those seen in [Figures 6, 7, and S1](#). ([28, 82](#))

The order of phase transformation and crystal growth, and mechanisms by which these processes occur, have important environmental impacts. Iron oxides play significant roles in the sequestration of arsenic and heavy metals, and understanding the release of these elements due to dissolution or their uptake during precipitation, phase transformation, and crystal growth will aid in making more accurate predictions about the fate and transport of these elements through the environment.

Conclusion

Several possible mechanisms for phase transformation and growth of hematite from 2InFh have been discussed. Low temperature magnetometry data demonstrate the presence of small, poorly crystalline hematite particles at very early aging times and support the hypothesis that small 2InFh particles first phase transform, then aggregate or serve as sites for aggregation of additional ferrihydrite. Measurements of remanent magnetization detected and identified hematite at lower concentrations and higher defect levels than the X-ray diffraction techniques used here. Evidence

was also seen for the rapid formation of large hematite particles, supporting the hypothesis of assembly followed by rapid transformation. Ultimately, we conclude that 2InFh undergoes phase transformation before assembly into larger particles but do not exclude the possibility that both of the proposed mechanisms operate simultaneously.

Supporting Information

The Supporting Information is available free of charge on the [ACS Publications website](#) at DOI: [10.1021/acs.cgd.5b01471](https://doi.org/10.1021/acs.cgd.5b01471).

- Preferential dissolution results for control experiments, transmission electron microscopy images of a hematite nanoparticle at nine tilt angles ([PDF](#))
- **PDF**
 - [cg5b01471_si_001.pdf \(357.29 kB\)](#)

Phase Transformation and Particle-Mediated Growth in the Formation of Hematite from 2-Line Ferrihydrite

[figshare](#)

Share [Download](#)

#Author Present Address

Physical Sciences Division, Pacific Northwest National Lab, Richland, WA 99352, United States.

Funding Information

Participation of J.A.S. and R.L.P. in this research is funded by the National Science Foundation (No. 0957696). J.A.S. also receives funding from the University of Minnesota IPrime Nanostructural Materials and Processes Program and the Department of Chemistry Newman and Lillian Bortnick Fellowship. Participation of J.M.F. and the Institute for Rock Magnetism in this research is funded by the NSF-EAR Instrumentation and Facilities #1339505. Participation of B.G. in this research is funded by the Director, Office of Science, Office of Basic Energy Sciences, of the U.S. Department of Energy (BES-DOE) under Contract No. DE-AC02-05CH11231. Work at the Advanced Photon Source was supported by DOE under Contract DEAC02-06CH11357.

The authors declare no competing financial interest.

-

Acknowledgment

We thank Valeri Petkov (Department of Physics, Central Michigan University) for assistance with synchrotron XRD/PDF experiments at the APS. Parts of this work were carried out in the Characterization Facility, University of Minnesota, a member of the NSF-funded Materials Research Facilities Network (www.mrfn.org) via the MRSEC program.

- [Reference QuickView](#)
-

References

This article references 82 other publications.

1. [1.](#)

Lovley, D. R. Microbial Fe(III) reduction in subsurface environments *FEMS Microbiol. Rev.* **1997**, 20, 305–313 DOI: 10.1111/j.1574-6976.1997.tb00316.x

[\[Crossref\]](#), [\[CAS\]](#)

2. [2.](#)

Nealson, K. H.; Myers, C. R. Microbial reduction of manganese and iron: new approaches to carbon cycling *Appl. Environ. Microbiol.* **1992**, 58, 439– 43

[\[PubMed\]](#), [\[CAS\]](#)

3. [3.](#)

DiChristina, T. J.; Fredrickson, J. K.; Zachara, J. M. Enzymology of electron transport: Energy generation with geochemical consequences *Rev. Mineral. Geochem.* **2005**, 59, 27– 52 DOI: 10.2138/rmg.2005.59.3

[\[Crossref\]](#), [\[CAS\]](#)

4. [4.](#)

Fortin, D.; Langley, S. Formation and occurrence of biogenic iron-rich minerals *Earth-Sci. Rev.* **2005**, 72, 1–19 DOI: 10.1016/j.earscirev.2005.03.002

[\[Crossref\]](#), [\[CAS\]](#)

5. [5.](#)

Cornell, R. M.; Schwertmann, U. *The Iron Oxides: Structures, Properties, Reactions, Occurrences and Uses*, 2nd ed.; Wiley-VCH: Weinheim, **2003**; p 664.

[\[Crossref\]](#)

6. [6.](#)

Erbs, J. J.; Berquó, T. S.; Reinsch, B. C.; Lowry, G. V.; Banerjee, S. K.; Penn, R. L. Reductive dissolution of arsenic-bearing ferrihydrite *Geochim. Cosmochim. Acta* **2010**, 74, 3382– 3395 DOI: 10.1016/j.gca.2010.01.033

[\[Crossref\]](#), [\[CAS\]](#)

7. [7.](#)

Stipp, S. L. S.; Hansen, M.; Kristensen, R.; Hochella, M. F., Jr; Bennedsen, L.; Dideriksen, K.; Balic-Zunic, T.; Léonard, D.; Mathieu, H. J. Behaviour of Fe-oxides relevant to contaminant uptake in the environment *Chem. Geol.* **2002**, 190, 321– 337 DOI: 10.1016/S0009-2541(02)00123-7

[\[Crossref\]](#), [\[CAS\]](#)

8. [8.](#)

Nedel, S.; Dideriksen, K.; Christiansen, B. C.; Bovet, N.; Stipp, S. L. S. Uptake and Release of Cerium During Fe-Oxide Formation and Transformation in Fe(II) Solutions *Environ. Sci. Technol.* **2010**, 44, 4493–4498 DOI: 10.1021/es9031503

[\[ACS Full Text\]](#) , [\[CAS\]](#)

9. [9.](#)

Usman, A. R. A.; Kuzyakov, Y.; Lorenz, K.; Stahr, K. Remediation of a soil contaminated with heavy metals by immobilizing compounds *J. Plant Nutr. Soil Sci.* **2006**, 169, 205– 212 DOI: 10.1002/jpln.200421685

[\[Crossref\]](#), [\[CAS\]](#)

10. [10.](#)

Ford, R. G.; Bertsch, P. M.; Farley, K. J. Changes in Transition and Heavy Metal Partitioning during Hydrous Iron Oxide Aging *Environ. Sci. Technol.* **1997**, 31, 2028– 2033 DOI: 10.1021/es960824+

[\[ACS Full Text\]](#) , [\[CAS\]](#)

11. [11.](#)

Cwiertny, D. M.; Handler, R. M.; Schaefer, M. V.; Grassian, V. H.; Scherer, M. M. Interpreting nanoscale size-effects in aggregated Fe-oxide suspensions: Reaction of Fe(II) with Goethite *Geochim. Cosmochim. Acta* **2008**, 72, 1365– 1380 DOI: 10.1016/j.gca.2007.12.018

[\[Crossref\]](#), [\[CAS\]](#)

12. [12.](#)

Jambor, J. L.; Dutrizac, J. E. Occurrence and Constitution of Natural and Synthetic Ferrihydrite, a Widespread Iron Oxyhydroxide *Chem. Rev.* **1998**, 98, 2549– 2586 DOI: 10.1021/cr970105t

[\[ACS Full Text\]](#), [\[CAS\]](#)

13. [13.](#)

Banfield, J. F.; Welch, S. A.; Zhang, H.; Thomsen Ebert, T.; Lee Penn, R. Aggregation-Based Crystal Growth and Microstructure Development in Natural Iron Oxyhydroxide Biomineralization Products *Science* **2000**, 289, 751– 754 DOI: 10.1126/science.289.5480.751

[\[Crossref\]](#), [\[PubMed\]](#), [\[CAS\]](#)

14. [14.](#)

Vikesland, P. J.; Valentine, R. L. Iron Oxide Surface-Catalyzed Oxidation of Ferrous Iron by Monochloramine: Implications of Oxide Type and Carbonate on Reactivity *Environ. Sci. Technol.* **2002**, 36, 512– 519 DOI: 10.1021/es010935v

[\[ACS Full Text\]](#), [\[CAS\]](#)

15. [15.](#)

Schwertmann, U. Solubility and dissolution of iron oxides *Plant Soil* **1991**, 130, 1– 25 DOI: 10.1007/BF00011851

[\[Crossref\]](#), [\[CAS\]](#)

16. [16.](#)

Navrotsky, A.; Mazeina, L.; Majzlan, J. Size-Driven Structural and Thermodynamic Complexity in Iron Oxides *Science* **2008**, 319, 1635– 1638 DOI: 10.1126/science.1148614

[\[Crossref\]](#), [\[PubMed\]](#), [\[CAS\]](#)

17. [17.](#)

Towe, K. M.; Bradley, W. F. Mineralogical constitution of colloidal “hydrous ferric oxides: *J. Colloid Interface Sci.* **1967**, 24, 384– 392 DOI: 10.1016/0021-9797(67)90266-4

[\[Crossref\]](#), [\[CAS\]](#)

18. [18.](#)

Michel, F. M.; Ehm, L.; Antao, S. M.; Lee, P. L.; Chupas, P. J.; Liu, G.; Strongin, D. R.; Schoonen, M. A. A.; Phillips, B. L.; Parise, J. B. The Structure of Ferrihydrite, a Nanocrystalline Material *Science* **2007**, 316, 1726– 1729 DOI: 10.1126/science.1142525

[\[Crossref\]](#), [\[PubMed\]](#), [\[CAS\]](#)

19. [19.](#)

Michel, F. M.; Barron, V.; Torrent, J.; Morales, M. P.; Serna, C. J.; Boily, J. F.; Liu, Q.; Ambrosini, A.; Cismasu, A. C.; Brown, G. E. Ordered ferrimagnetic form of ferrihydrite reveals links among structure, composition, and magnetism *Proc. Natl. Acad. Sci. U. S. A.* **2010**, 107, 2787– 2792 DOI: 10.1073/pnas.0910170107

[\[Crossref\]](#), [\[PubMed\]](#), [\[CAS\]](#)

20. [20.](#)

Manceau, A. Evaluation of the structural model for ferrihydrite derived from real-space modelling of high-energy X-ray diffraction data *Clay Miner.* **2009**, 44, 19– 34 DOI: 10.1180/claymin.2009.044.1.19

[\[Crossref\]](#), [\[CAS\]](#)

21. [21.](#)

Manceau, A. PDF analysis of ferrihydrite and the violation of Pauling's Principia *Clay Miner.* **2010**, 45, 225–228 DOI: 10.1180/claymin.2010.045.2.225

[\[Crossref\]](#), [\[CAS\]](#)

22. [22.](#)

Rancourt, D. G.; Meunier, J. F. Constraints on structural models of ferrihydrite as a nanocrystalline material *Am. Mineral.* **2008**, 93, 1412– 1417 DOI: 10.2138/am.2008.2782

[\[Crossref\]](#), [\[CAS\]](#)

23. [23.](#)

Gilbert, B.; Erbs, J. J.; Penn, R. L.; Petkov, V.; Spagnoli, D.; Waychunas, G. A. A disordered nanoparticle model for 6-line ferrihydrite *Am. Mineral.* **2013**, 98, 1465– 1476 DOI: 10.2138/am.2013.4421

[\[Crossref\]](#), [\[CAS\]](#)

24. [24.](#)

Janney, D. E.; Cowley, J. M.; Buseck, P. R. Transmission electron microscopy of synthetic 2- and 6-line ferrihydrite *Clays Clay Miner.* **2000**, 48, 111– 119 DOI: 10.1346/CCMN.2000.0480114

[\[Crossref\]](#), [\[CAS\]](#)

25. [25.](#)

Janney, D. E.; Cowley, J. M.; Buseck, P. R. Structure of synthetic 2-line ferrihydrite by electron nanodiffraction *Am. Mineral.* **2000**, 85, 1180– 1187 DOI: 10.2138/am-2000-8-910

[\[Crossref\]](#), [\[CAS\]](#)

26. [26.](#)

Jansen, E.; Kyek, A.; Schäfer, W.; Schwertmann, U. The structure of six-line ferrihydrite *Appl. Phys. A: Mater. Sci. Process.* **2002**, 74, S1004– S1006 DOI: 10.1007/s003390101175

[\[Crossref\]](#), [\[CAS\]](#)

27. [27.](#)

Figueiredo, M. O.; Silva, T. P.; Veiga, J. P. Natural nanomaterials: reappraising the elusive structure of the nano-sized mineral ferrihydrite through X-ray absorption spectroscopy at the iron K-edge *Mater. Sci. Forum* **2012**, 730-732, 931– 935 DOI: 10.4028/www.scientific.net/MSF.730-732.931

[\[Crossref\]](#)

28. [28.](#)

Soltis, J. A.; Penn, R. L., Oriented attachment and non-classical formation in iron oxides. In *Iron Oxides*; Faivre, D., Ed.; Wiley VCH: Weinheim, **2015**.

29. [29.](#)

Zhang, H.; Banfield, J. F. New kinetic model for the nanocrystalline anatase-to-rutile transformation revealing rate dependence on number of particles *Am. Mineral.* **1999**, 84, 528– 535

[\[Crossref\]](#), [\[CAS\]](#)

30. [30.](#)

Penn, R. L.; Banfield, J. F. Oriented attachment and growth, twinning, polytypism, and formation of metastable phases: Insights from nanocrystalline TiO₂ *Am. Mineral.* **1998**, 83, 1077– 1082

[\[Crossref\]](#), [\[CAS\]](#)

31. [31.](#)


Penn, R. L. Kinetics of Oriented Aggregation *J. Phys. Chem. B* **2004**, 108, 12707– 12712 DOI: 10.1021/jp036490+

[\[ACS Full Text\]](#) , [\[CAS\]](#)

32. [32.](#)

Penn, R. L.; Banfield, J. F. Imperfect Oriented Attachment: Dislocation Generation in Defect-Free Nanocrystals *Science* **1998**, 281, 969– 971 DOI: 10.1126/science.281.5379.969

[\[Crossref\]](#), [\[PubMed\]](#), [\[CAS\]](#)

33. [33.](#)
Song, R.-Q.; Cölfen, H. Mesocrystals-Ordered Nanoparticle Superstructures *Adv. Mater.* **2010**, 22, 1301–1330 DOI: 10.1002/adma.200901365
[\[Crossref\]](#), [\[PubMed\]](#), [\[CAS\]](#)
34. [34.](#)
Nespolo, M.; Ferraris, G. The oriented attachment mechanism in the formation of twins – a survey *Eur. J. Mineral.* **2004**, 16, 401– 406 DOI: 10.1127/0935-1221/2004/0016-0401
[\[Crossref\]](#), [\[CAS\]](#)
35. [35.](#)
Niederberger, M.; Colfen, H. Oriented attachment and mesocrystals: Non-classical crystallization mechanisms based on nanoparticle assembly *Phys. Chem. Chem. Phys.* **2006**, 8, 3271– 3287 DOI: 10.1039/b604589h
[\[Crossref\]](#), [\[PubMed\]](#), [\[CAS\]](#)
36. [36.](#)
Zeng, H. C. Oriented attachment: a versatile approach for construction of nanomaterials *Int. J. Nanotechnol.* **2007**, 4, 329– 346 DOI: 10.1504/IJNT.2007.013970
[\[Crossref\]](#), [\[CAS\]](#)
37. [37.](#)
Zhang, H.; Penn, R. L.; Lin, Z.; Cölfen, H. Nanocrystal growth via oriented attachment *CrystEngComm* **2014**, 16, 1407 DOI: 10.1039/c4ce90001d
[\[Crossref\]](#), [\[CAS\]](#)
38. [38.](#)
Penn, R. L.; Oskam, G.; Strathmann, T. J.; Searson, P. C.; Stone, A. T.; Veblen, D. R. Epitaxial Assembly in Aged Colloids *J. Phys. Chem. B* **2001**, 105, 2177– 2182 DOI: 10.1021/jp003570u
[\[ACS Full Text\]](#) , [\[CAS\]](#)
39. [39.](#)
Park, J.-I.; Jun, Y.-w.; Choi, J.-s.; Cheon, J. Highly crystalline anisotropic superstructures via magnetic field induced nanoparticle assembly *Chem. Commun.* **2007**, 5001– 5003 DOI: 10.1039/b712513e
[\[Crossref\]](#), [\[PubMed\]](#), [\[CAS\]](#)
40. [40.](#)

Baynton, A.; Radomirovic, T.; Ogden, M. I.; Raston, C. L.; Richmond, W. R.; Jones, F. Small molecules induce mesocrystal formation: nanoparticle aggregation directed by self-assembling calixarenes *CrystEngComm* **2011**, 13, 109– 112 DOI: 10.1039/C0CE00579G

[\[Crossref\]](#), [\[CAS\]](#)

41. [41.](#)

Liu, Z.; Wen, X. D.; Wu, X. L.; Gao, Y. J.; Chen, H. T.; Zhu, J.; Chu, P. K. Intrinsic Dipole-Field-Driven Mesoscale Crystallization of Core–Shell ZnO Mesocrystal Microspheres *J. Am. Chem. Soc.* **2009**, 131, 9405– 9412 DOI: 10.1021/ja9039136

[\[ACS Full Text\]](#) , [\[CAS\]](#)

42. [42.](#)

Yuwono, V.; Burrows, N. D.; Soltis, J. A.; Penn, R. L. Oriented Aggregation: Formation and Transformation of Mesocrystal Intermediates Revealed *J. Am. Chem. Soc.* **2010**, 132, 2163– 2165 DOI: 10.1021/ja909769a

[\[ACS Full Text\]](#) , [\[CAS\]](#)

43. [43.](#)

Fang, X.-L.; Chen, C.; Jin, M.-S.; Kuang, Q.; Xie, Z.-X.; Xie, S.-Y.; Huang, R.-B.; Zheng, L.-S. Single-crystal-like hematite colloidal nanocrystal clusters: synthesis and applications in gas sensors, photocatalysis and water treatment *J. Mater. Chem.* **2009**, 19, 6154 DOI: 10.1039/b905034e

[\[Crossref\]](#), [\[CAS\]](#)

44. [44.](#)

Sabyrov, K.; Penn, R. L. Interface-mediated phase transformation in nanocrystalline particles: the case of the TiO₂ allotropes *CrystEngComm* **2015**, 17, 2062– 2069 DOI: 10.1039/C4CE02138J

[\[Crossref\]](#), [\[CAS\]](#)

45. [45.](#)

Sabyrov, K.; Penn, R. L. A kinetic model for two-step phase transformation of hydrothermally treated nanocrystalline anatase. In preparation, **2015**.

46. [46.](#)

Zhang, H.; Banfield, J. F. Phase transformation of nanocrystalline anatase-to-rutile via combined interface and surface nucleation *J. Mater. Res.* **2000**, 15, 437– 448 DOI: 10.1557/JMR.2000.0067

[\[Crossref\]](#), [\[CAS\]](#)

47. [47.](#)

Das, S.; Hendry, M. J.; Essilfie-Dughan, J. Transformation of Two-Line Ferrihydrite to Goethite and Hematite as a Function of pH and Temperature *Environ. Sci. Technol.* **2011**, 45, 268– 275 DOI: 10.1021/es101903y

[\[ACS Full Text\]](#), [\[CAS\]](#)

48. [48.](#)

Shaw, S.; Pepper, S. E.; Bryan, N. D.; Livens, F. R. The kinetics and mechanisms of goethite and hematite crystallization under alkaline conditions, and in the presence of phosphate *Am. Mineral.* **2005**, 90, 1852–1860 DOI: 10.2138/am.2005.1757

[\[Crossref\]](#), [\[CAS\]](#)

49. [49.](#)

Ray, J. R.; Wan, W.; Gilbert, B.; Jun, Y.-S. Effects of Formation Conditions on the Physicochemical Properties, Aggregation, and Phase Transformation of Iron Oxide Nanoparticles *Langmuir* **2013**, 29, 1069–1076 DOI: 10.1021/la3034319

[\[ACS Full Text\]](#), [\[CAS\]](#)

50. [50.](#)

Vu, H. P.; Shaw, S.; Benning, L. G. Transformation of ferrihydrite to hematite: an in situ investigation on the kinetics and mechanisms *Mineral. Mag.* **2008**, 72, 217– 220 DOI: 10.1180/minmag.2008.072.1.217

[\[Crossref\]](#), [\[CAS\]](#)

51. [51.](#)

Cornell, R. M.; Giovanoli, R. Effect of solution conditions on the proportion and morphology of goethite formed from ferrihydrite *Clays Clay Miner.* **1985**, 33, 424– 432 DOI: 10.1346/CCMN.1985.0330508

[\[Crossref\]](#), [\[CAS\]](#)

52. [52.](#)

Schwertmann, U.; Murad, E. Effect of pH on the formation of goethite and hematite from ferrihydrite *Clays Clay Miner.* **1983**, 31, 277– 284 DOI: 10.1346/CCMN.1983.0310405

[\[Crossref\]](#), [\[CAS\]](#)

53. [53.](#)

Burrows, N. D.; Hale, C. R. H.; Penn, R. L. Effect of pH on the Kinetics of Crystal Growth by Oriented Aggregation *Cryst. Growth Des.* **2013**, 13, 3396– 3403 DOI: 10.1021/cg4001939

[\[ACS Full Text\]](#), [\[CAS\]](#)

54. [54.](#)

Burrows, N. D.; Hale, C. R. H.; Penn, R. L. Effect of Ionic Strength on the Kinetics of Crystal Growth by Oriented Aggregation *Cryst. Growth Des.* **2012**, 12, 4787– 4797 DOI: 10.1021/cg3004849

[\[ACS Full Text\]](#), [\[CAS\]](#)

55. [55.](#)

Cornell, R. M. Effect of simple sugars on the alkaline transformation of ferrihydrite into goethite and hematite *Clays Clay Miner.* **1985**, 33, 219– 227 DOI: 10.1346/CCMN.1985.0330308

[\[Crossref\]](#), [\[CAS\]](#)

56. [56.](#)

Cornell, R. M.; Schwertmann, U. Influence of organic anions on the crystallization of ferrihydrite *Clays Clay Miner.* **1979**, 27, 402– 410 DOI: 10.1346/CCMN.1979.0270602

[\[Crossref\]](#), [\[CAS\]](#)

57. [57.](#)

Fischer, W. R.; Schwertmann, U. The Formation of Hematite from Amorphous Iron(III) Hydroxide *Clays Clay Miner.* **1975**, 23, 33– 37 DOI: 10.1346/CCMN.1975.0230105

[\[Crossref\]](#), [\[CAS\]](#)

58. [58.](#)

Burleson, D. J.; Penn, R. L. Two-Step Growth of Goethite from Ferrihydrite *Langmuir* **2006**, 22, 402– 409 DOI: 10.1021/la051883g

[\[ACS Full Text\]](#), [\[CAS\]](#)

59. [59.](#)

Frandsen, C.; Legg, B. A.; Comolli, L. R.; Zhang, H.; Gilbert, B.; Johnson, E.; Banfield, J. F. Aggregation-induced growth and transformation of β -FeOOH nanorods to micron-sized α -Fe₂O₃ spindles *CrystEngComm* **2014**, 16, 1451– 1458 DOI: 10.1039/C3CE40983J

[\[Crossref\]](#), [\[CAS\]](#)

60. [60.](#)

Navrotsky, A. Energetics of oxide nanoparticles *Int. J. Quantum Chem.* **2009**, 109, 2647– 2657 DOI: 10.1002/qua.21981

[\[Crossref\]](#), [\[CAS\]](#)

61. [61.](#)

Penn, R. L.; Erbs, J.; Gulliver, D. Controlled growth of alpha-FeOOH nanorods by exploiting-oriented aggregation *J. Cryst. Growth* **2006**, 293, 1– 4 DOI: 10.1016/j.jcrysgro.2006.05.005

[\[Crossref\]](#), [\[CAS\]](#)

62. [62.](#)

Sabyrov, K.; Burrows, N. D.; Penn, R. L. Size-Dependent Anatase to Rutile Phase Transformation and Particle Growth *Chem. Mater.* **2013**, 25, 1408– 1415 DOI: 10.1021/cm302129a

[\[ACS Full Text\]](#), [\[CAS\]](#)

63. [63.](#)

Bilardello, D.; Jackson, M., What do the Mumpsies do? *IRM Q. Fall* **2013**, 23.

64. [64.](#)

Bowles, J.; Jackson, M.; Banerjee, S. K., Interpretation of Low-Temperature Data Part II: The Hematite Morin Transition. *IRM Q. Spring* **2010**, 20.

65. [65.](#)

Özdemir, Ö.; Dunlop, D. J.; Berquó, T. S. Morin transition in hematite: Size dependence and thermal hysteresis *Geochem., Geophys., Geosyst.* **2008**, 9, Q10Z01 DOI: 10.1029/2008GC002110

[\[Crossref\]](#)

66. [66.](#)

Feinberg, J. M.; Solheid, P. A.; Swanson-Hysell, N. L.; Jackson, M. J.; Bowles, J. A. Full vector low-temperature magnetic measurements of geologic materials *Geochem., Geophys., Geosyst.* **2015**, 16, 301–314 DOI: 10.1002/2014GC005591

[\[Crossref\]](#)

67. [67.](#)

Schwertmann, U.; Cornell, R. M. *Iron Oxides in the Laboratory: Preparation and Characterization*, 2nd ed.; Wiley-VCH: Weinheim, **2000**.

[\[Crossref\]](#)

68. [68.](#)

Kukkadapu, R.; Zachara, J. M.; Fredrickson, J. K.; Smith, S. C.; Dohnalkova, A. C.; Russell, C. K. Transformation of 2-line ferrihydrite to 6-line ferrihydrite under oxic and anoxic conditions *Am. Mineral.* **2003**, 88, 1903 DOI: 10.2138/am-2003-11-1233

[\[Crossref\]](#), [\[CAS\]](#)

69. [69.](#)

Zhao, J.; Huggins, F. E.; Feng, Z.; Huffman, G. P. Ferrihydrite: Surface structure and its effects on phase transformation *Clays Clay Miner.* **1994**, 42, 737– 746

[\[Crossref\]](#), [\[CAS\]](#)

70. [70.](#)

Scherrer, P. *Nachrichten von der Gesellschaft der Wissenschaften zu Göttingen, mathematisch-physikalische Klasse* **1918**, 2, 96

71. [71.](#)

Sabyrov, K.; Adamson, V.; Penn, R. L. Two-step phase transformation of anatase to rutile in aqueous suspension *CrystEngComm* **2014**, 16, 1488 DOI: 10.1039/C3CE41820K

[\[Crossref\]](#), [\[CAS\]](#)

72. [72.](#)

Hammersley, A. P. FIT2D: An Introduction and Overview, ESRF: Grenoble, France, **1997**.

73. [73.](#)

Burt, R. *Soil Survey Laboratory Methods Manual*, 4th ed.; United States Department of Agriculture Natural Resources Conservation Service: Washington, DC, **2004**; Vol. 42.

74. [74.](#)

Schwertmann, U. Use of Oxalate for Fe Extraction from Soils *Can. J. Soil Sci.* **1973**, 53, 244– 246 DOI: 10.4141/cjss73-037

[\[Crossref\]](#), [\[CAS\]](#)

75. [75.](#)

Dominik, P.; Kaupenjohann, M. Simple spectrophotometric determination of Fe in oxalate and HCl soil extracts *Talanta* **2000**, 51, 701– 707 DOI: 10.1016/S0039-9140(99)00324-0

[\[Crossref\]](#), [\[PubMed\]](#), [\[CAS\]](#)

76. [76.](#)

Rasband, W. S. *ImageJ*; U. S. National Institutes of Health: Bethesda, Maryland, USA, **1997–2015**.

77. [77.](#)

Guyodo, Y.; Banerjee, S.; Leepenn, R.; Burleson, D.; Berquo, T.; Seda, T.; Solheid, P. Magnetic properties of synthetic six-line ferrihydrite nanoparticles *Phys. Earth Planet. Inter.* **2006**, 154, 222– 233 DOI: 10.1016/j.pepi.2005.05.009

[\[Crossref\]](#), [\[CAS\]](#)

78. [78.](#)

Berquó, T. S.; Erbs, J. J.; Lindquist, A.; Penn, R. L.; Banerjee, S. K. Effects of magnetic interactions in antiferromagnetic ferrihydrite particles *J. Phys.: Condens. Matter* **2009**, 21, 176005 DOI: 10.1088/0953-8984/21/17/176005

[\[Crossref\]](#), [\[PubMed\]](#), [\[CAS\]](#)

79. [79.](#)

Özdemir, Ö.; Dunlop, D. J. Hysteresis and coercivity of hematite *J. Geophysical Res.: Solid Earth* **2014**, 119,2582– 2594 DOI: 10.1002/2013JB010739

[\[Crossref\]](#)

80. [80.](#)

Bhattacharjee, A.; Rooj, A.; Roy, M.; Kusz, J.; Gütlich, P. Solventless synthesis of hematite nanoparticles using ferrocene *J. Mater. Sci.* **2013**, 48, 2961– 2968 DOI: 10.1007/s10853-012-7067-x

[\[Crossref\]](#), [\[CAS\]](#)

81. [81.](#)

Penn, R. L.; Soltis, J. A. Characterizing crystal growth by oriented aggregation *CrystEngComm* **2014**, 16,1409– 1418 DOI: 10.1039/c3ce41773e

[\[Crossref\]](#), [\[CAS\]](#)

82. [82.](#)

Li, D.; Nielsen, M. H.; Lee, J. R.; Frandsen, C.; Banfield, J. F.; De Yoreo, J. J. Direction-specific interactions control crystal growth by oriented attachment--SI *Science* **2012**, 336, 1014– 8 DOI: 10.1126/science.1219643

[\[Crossref\]](#), [\[PubMed\]](#), [\[CAS\]](#)